1	
2	
3	Stratospheric chlorine processing after the 2020 Australian wildfires derived from satellite data
5	
6	Peidong Wang, Susan Solomon, Kane Stone
7 8	Department of Earth, Atmospheric, and Planetary Sciences, Massachusetts Institute of Technology, Cambridge, MA, USA
9	*Peidong Wang
10	Email: pdwang@mit.edu
11 12	<b>Author Contributions:</b> P.W., S.S. designed research; P.W., K.S. performed research; P.W. analyzed data; P.W., S.S., K.S. wrote the paper.
13	Competing Interest Statement: The authors declare no compete of interest.
14	Classification: Physical Sciences-Earth, Atmospheric, and Planetary Sciences
15	Keywords: stratospheric ozone, chlorine activation, wildfire
16	
17	This PDF file includes:
18 19 20	Main Text Figures 1 to 6 Figures S1 to S9

#### Abstract

21

39

49 50

51 52

53 54

55

56

57 58

59

60

61

62

63

64

65 66

67

68

69

70

71

22 The 2019 – 2020 Australian summer wildfires injected an amount of organic gases and particles 23 into the stratosphere unprecedented in the satellite record since 2002, causing large unexpected 24 changes in HCl and ClONO2. These fires provided a novel opportunity to evaluate heterogeneous 25 reactions on organic aerosols in the context of stratospheric chlorine and ozone depletion 26 chemistry. It has long been known that heterogeneous chlorine (CI) activation occurs on the polar stratospheric clouds (PSCs; liquid and solid particles containing water, sulfuric acid, and in some 27 28 cases nitric acid) that are found in the stratosphere, but these are only effective for ozone depletion 29 chemistry at temperatures below about 195 K (i.e., largely in the polar regions during winter). Here, 30 we develop a new approach to quantitatively assess atmospheric evidence for these reactions 31 using satellite data. We show that heterogeneous reactions apparently even happened at 32 temperatures above 220 K during autumn on the organic aerosols present in 2020, in contrast to 33 earlier years. Further, increased variability in HCl was also found after the wildfires, suggesting 34 diverse chemical properties among the 2020 aerosols. We also confirm the expectation based upon 35 laboratory studies that heterogeneous CI activation has a strong dependence upon water vapor 36 partial pressure and hence atmospheric altitude, becoming much faster close to the tropopause. 37 Our analysis improves the understanding of heterogeneous reactions that are important for 38 stratospheric ozone chemistry under both background and wildfire conditions.

# Significance Statement

Heterogeneous chlorine activation is a major driver for stratospheric ozone depletion and is 41 understood to happen on polar stratospheric clouds (PSCs) at temperatures below about 195 K. 42 The 2020 Australian wildfire released large amounts of organic aerosols, whose chemical 43 properties under stratospheric conditions are virtually unknown. Here, we developed a novel 44 approach to analyze the temperature dependency of atmospheric chlorine heterogeneous 45 chemistry using satellite data. We found that such reactions can happen at temperatures even 46 above 220 K on wildfire aerosols in 2020. Organic aerosols are present to some degree in the lower 47 stratosphere even under background conditions. This result indicates that CI processes on organic aerosols likely need to be considered in future stratospheric ozone simulations.

## **Main Text**

#### Introduction

The Australian wildfire black summer was the largest such event in the satellite era. It produced on the order of 1 Tg of aerosols in the stratosphere from about Dec 31, 2019 to Jan 5, 2020 (1), equivalent to a small volcanic eruption. These aerosols and their precursors are brought into the lower stratosphere by pyrocumulonimbus convection, where they can be expected to decay over time. Volcanic aerosols typically display an e-folding time of about 18 months (2, 3). Model simulations (which assumed wildfire-released aerosols behave like sulfuric acid and water particles) (4), satellite observations (5–7), and *in-situ* measurements (8) all found significant ozone decreases in the lower stratosphere at southern hemisphere mid-latitudes in 2020 after the wildfire. Unusually low ozone abundances even continued into 2021 (6, 9). While there is evidence for some dynamical contributions to the ozone variations observed in that year (6, 10), averaged mid-latitude values presented in (6) indicate record low local abundances near 20 km, suggesting additional chemistry is likely. In addition, unprecedented and completely unexpected changes in mid-latitude chlorine (CI) reservoir species (HCI and CIONO2) were also found in satellite and in-situ observations (6-8), suggestive of CI surface chemistry, e.g., via the following heterogeneous reaction of HCl + ClONO<sub>2</sub> → Cl<sub>2</sub> + HNO<sub>3</sub> (11). The Cl<sub>2</sub> subsequently photolyzes rapidly in sunlit air, and can form CI and CIO which deplete ozone. The fingerprint of N2O5 hydrolysis, another key heterogeneous reaction that contributes to depletion in the ozone laver, was also found in the satellite data (12) but cannot explain the unusual changes in HCl and ClONO2. Here we provide a fresh approach to the analysis of the Cl chemistry inspired by the unexpected HCl and ClONO<sub>2</sub> 73 data that sheds light on its temperature-dependent chemistry not only for wildfires but also for 74 background conditions.

Laboratory measurements (13, 14), *in-situ* observations (15), and model simulation (16) all suggest that the heterogeneous CI reaction between HCl and ClONO<sub>2</sub> is only effective on the 77 surfaces of typical stratospheric aerosols at temperatures below 195 K. In contrast to stratospheric

58 background sulfuric acid and water aerosols, wildfire-released particles contain a wide variety of 59 organic compounds (17, 18), which could have different chemical properties. Limited laboratory 80 50 studies suggest that organic aerosols can enhance HCl uptake (19) and at warmer temperatures 81 50 (20).

The new approach presented here quantifies the temperature for CI activation using 83 satellite data from ACE-FTS (Atmospheric Chemistry Experiment-Fourier Transform Spectrometer; 84 ACE for short) (21) combined with temperatures from a back trajectory model named Lagranto 85 (Lagrangian Analysis Tool) (22), driven by meteorological conditions from ERA5 (European Centre 86 for Medium-Range Weather Forecasts) reanalysis data (23). We focus on the southern hemisphere 87 midlatitudes defined as  $40-55\,^{\circ}$ S and polar vortex region defined as  $65-90\,^{\circ}$ S. The most 88 significant changes in HCl and ClONO2 in 2020 are observed at altitude ranges between  $15-22\,^{\circ}$ 

km (Fig. S1). Unless otherwise specified, we mainly focus on 18.5 km in our analysis to maximize the effects.

#### Results

90

91 92

93 94

95 96

97

98

99

100

101

102

112

113

114

115

117

## Separating dynamical and chemical processes

Fig. 1A shows the monthly mean ACE data for CO (an indicator of biomass burning) at the lower stratosphere mid-latitudes. CO in 2020 reached a record high (6, 7), suggesting a significant amount of biomass burning and its long-lasting effect continuing throughout the entire year. CO in 2021 is within the range of climatology, indicating no significant wildfire or new particles injected into the lower stratosphere in that year. 2012 is also highlighted in Fig. 1 since we use it here as a typical reference year in later analysis, given no known large volcanic eruptions nor big biomass burning events in that year.

While HCl displayed remarkable anomalies in 2020, HF was within the range of past years, 104 confirming the role of chemistry (Fig. 1). Once anthropogenically produced CFCs 105 (chlorofluorocarbons) reach the stratosphere, they decompose into the fluorine (Fy) and chlorine 106 (Cly) families of compounds. Nearly all of the Fy is in the form of HF because there are no known 107 chemical loss pathways of HF in the stratosphere; hence it has long been used as an inactive tracer 108 (24, 25). Insofar as the breakdown of CFCs is the dominant source of both stratospheric chlorine 109 and fluorine, Cly and Fy should be proportional to one another. Viewed in this context, HCl and HF 110 behavior also suggests unusual chemistry lasting into 2021, but with much smaller magnitude than 111 2020.

Correlation between chemical species or "tracer-tracer" analysis is a powerful tool to analyze dynamical and chemical interactions (26–28). The basis of the analysis is that dynamical transport should affect inactive and active species similarly, so departures from correlation in the active species are indicative of chemical processes. The availability of simultaneous ACE 116 observations of HF, HCl, and ClONO<sub>2</sub> along a common line of sight ensures consistency and is key to such an analysis. To separate dynamical from chemical effects on specific Cly species, we 118 perform the tracer-tracer analysis between HF and HCl, ClONO<sub>2</sub>, and their sum (Fig. 2 for mid-119 latitude and Fig. S2 for the polar region).

Fig. 2 shows tracer-tracer scatter plots of ACE HF and HCl, CIONO<sub>2</sub>, and HCl+CIONO<sub>2</sub> in each month from March to July. This spans months when no or little heterogeneous chemistry 122 normally occurs (~March-April) to months with rapid chemistry on PSCs in polar regions (June-123 July) and in between (May). All the data align on a nearly straight line in March, suggesting little or 124 no chemistry in this month. We therefore construct a baseline relationship between HF and the Cly

species from March 2004 – 2019 data using linear regression (indicated by the dark solid lines in 126 Fig. 2 and Fig. S2).

127 The shaded regions in Fig. 2 and Fig. S2 quantify the baseline uncertainty. There are 128 mainly two types of uncertainties in such analysis, one is the instrumental bias, and the other is the 129 interannual variability. As the tracer-tracer correlation mainly focuses on the relative difference of 130 to HF, which are measured by ACE at the same occultation, instrumental bias on both 131

molecules will largely cancel. To quantify the uncertainty of interannual variability and noise, we construct a baseline for each year in 2004 – 2019 to represent the range of variability in baselines. The shading areas indicate a conservative full range of variability bounded by the maximum and minimum baselines using data in individual years.

135 ACE has limited data coverage. To validate whether the results are robust, we compare 136 ACE (at 18.5 km) with the MLS (Microwave Limb Sounder at 68.2 hPa) in Figs. S3 and S4 (mid-137 latitude and polar vortex region, respectively) for tracer-tracer analysis between N2O and HCI (since 138 MLS does not have measurements for HF and CIONO<sub>2</sub>). MLS has much more spatial coverage, 139 with a lower signal-to-noise ratio on individual points (as shown in Figs. S3C and S4C). The 140 zonally averaged MLS data (Figs. S3B and S4B) agree well with ACE (Figs. S3A and S4A), 141 suggesting that even though ACE coverage is limited, it is consistent with MLS regarding the

changes in HCl from tracer-tracer analysis. Note that the zonal averaging process in MLS reduces the noise but it also clusters measurements towards the mean values. Therefore, the baseline slope becomes more sensitive to small changes in N<sub>2</sub>O and HCl in the clustered region, and the uncertainty range expands at those values where no or few data are fed into the linear regression. MLS N<sub>2</sub>O also has experienced a ~3% instrumental drift in the past decade, which could also 147 broaden the spread of the baseline uncertainty range (29). We therefore focus on the results from ACE measurements.

Fig. 2 shows that substantial deviations in HCl and ClONO2 from their respective "no-150" chemistry" baseline occur in July for every year, indicating the known CI activation mechanism on 151 PSCs (11). More important, in 2020, HCl and ClONO2 start to deviate from the "no-chemistry" 152 baseline even in March, when the temperature is far too warm for heterogeneous CI reactions to 153 happen on PSCs. HCl and ClONO2 in 2021 also display some deviations from the "no-chemistry" 154 baseline, but the magnitudes are considerably smaller than in 2020.

155 Interestingly, the decrease in HCl is roughly compensated by increases in ClONO2 in both 156 2020 and 2021 (e.g. April and May in Fig. 2 and Fig. S2, respectively) and in other years. The 157 decrease in HCl suggests that anomalous heterogeneous Cl reactions occurred in these two years. 158 However, at these latitudes outside the polar vortex, ample solar radiation is available to drive 159 HNO<sub>3</sub> photolysis (and reaction with OH also occurs), making NO<sub>2</sub> available to deactivate the 160 activated CI, forming CIONO2. With a rich supply of NO2, the net reaction thus largely transfers HCl 161 CIONO2. Similar CI deactivation forms the CIONO2 "collar" (30), a slice of enhanced CIONO2 162 surrounding the polar vortex in late spring as noted in past literature. Fig. 3 shows May HCl and 163 CIONO2 anomalies in 2020 compared to the May climatology from 2004 - 2019. The figure makes 164 clear that the CIONO<sub>2</sub> "collar" mechanism is significantly enhanced in 2020 as early as May, as

more CI has been converted from HCI into CIONO2 on wildfire-released particles. Similar processes continued to occur in 2021, but with a smaller magnitude (Fig. S5). HCl and ClONO2 are both considered to be reservoirs for active chlorine species that deplete ozone (mainly Cl and ClO). It may be useful to consider such a process to represent CI processing instead of CI activation, since the sum of HCl+ClONO2 is nearly conserved. Nonetheless, a small amount of enhanced ClO will be present as well, since CIONO2 and CIO are essentially in photochemical balance in the sunlit atmosphere, and enhanced CIONO2 therefore implies enhanced CIO and associated ozone loss. Indeed, evidence of enhanced CIO has been shown in both ACE and MLS measurements (6, 7).

## CI processing in the mid-latitudes

125

132

133

134

142 143

144

145

146

148

165

166 167

168

169

170

171 172

173 174

175 176

177 178

To estimate the temperatures that are likely to drive the heterogeneous chemistry, we first calculate the deviation of each data point in Fig. 2 from the "no-chemistry" baseline as a function of ACE-measured temperature (Fig. 4A-C). Thick lines show the averages of data points in 2 K temperature bins from the baseline that is constructed by all available data from 2004-2019. The shaded regions represent the full range of CI deviation from individual "no-chemistry" baselines that are constructed from data in individual years, representing the uncertainty due to variability. 182 Negative values in CIONO2 at warmer temperatures indicate that available CIO has been 183 deactivated to form CIONO2, and the sum of HCI and CIONO2 in Fig. 4C thus indicates that a large amount of the CI activated from HCI in 2020 and 2021 has almost all formed CIONO2 at warmer temperatures. As we focus on 40-55 °S where the temperature is well above 195 K, activation on the PSCs is not likely to take place. This is supported by the 2004-2019 climatology, in which the average CI activation remains close to zero. However, HCI data in 2020 and 2021 suggest that significant CI activation occurred at temperatures even well above 220 K, but not in any other years (although the magnitude of CI activation in 2021 is smaller than in 2020).

However, one pitfall of Figs. 2 and 4A-C is that the temperatures shown reflect only the state of the atmosphere at the satellite overpass, while CI activation could have occurred at a 192 different temperature along air parcel trajectories. We therefore use Lagranto (22) driven by ERA5 193 (23) to evaluate 5-day back trajectories for each data point in 2020 and 2021, as well as the 194 reference year of 2012. The radiative relaxation time for the lower stratosphere is on the order of 195 20 – 30 days (31, 32); we pick a rather conservative estimate of 5 days to avoid potential effects of

radiatively-driven ascent/descent of particles in the stratosphere. The ACE-measured instantaneous temperature is then replaced with the minimum temperature from the 5-day back trajectories of each data point (referred to as ERA5 T<sub>min</sub> in Fig. 4D-F), providing an estimate of the air parcel's recent minimum temperature exposure. ERA5 temperatures at the co-located ACE observations agree well with each other (Fig. S6), and we find that the 5-day minimum temperature is rather insensitive to small perturbations in the starting position (Fig. S7). We also verified that the minimum temperature is similar between 5-day and 10-day back trajectories for the air parcels released at 18.5 km (detailed discussion in the **Altitude-dependent CI activation** section). Back trajectories going beyond 10-days would require calculation of the air parcel's radiative field 205 including the effect of the wildfire particles and thus was not considered in this analysis.

Fig. 4D-F shows CI activation as a function of the 5-day minimum temperature calculated from Lagranto. The 5-day minimum temperature exposure for these measurements is still mainly above 195 K. This further strengthens the idea that wildfire-released organic aerosols can allow heterogeneous reactions to happen at warmer temperatures, which differs from the PSC 210 mechanism that requires the temperature to be lower than 195 K. Further, the PDFs shown in Fig. 4D-F for temperatures  $\geq$  195 K indicate that not only do 2020 and 2021 have different mean values than in 2012, but the spread after the wildfire is also much wider than that in 2012. One plausible explanation for this behavior is variability in the composition and/or abundances of organic aerosols from the wildfire, displaying different chemical properties. Note that the PDF for the sum of 215 HCI+CIONO2 is centered very close to zero for 2012 but displays a distinct offset from zero in 2020 and to a lesser extent in 2021, indicating significant enhancements in other species including e.g. HOCI (7) and CIO in those years only (6).

### CI processing in the polar vortex region

Fig. 5 shows CI activation in the polar vortex region at  $65-90\,^{\circ}$ S. CI activation for the total Cly in 2012 shows a sharp transition at 195 K (Fig. 5F), which matches remarkably well with the current understanding of CI activation on PSCs as first observed with aircraft methods (15). It is noteworthy that even in 2012 when the background CO and aerosol extinctions are at the lower end in the climatology, there is still some CIONO2 being converted from HCI at temperatures 226 between 195-205 K (Fig. 5D-E). Observations show that organic aerosols are widespread in the lower stratosphere. Among other sources, tropical biomass burning produces organic aerosols in the upper troposphere (33) that may be transported into the stratosphere. Thus, early-season CI processing on organic aerosols could occur to some extent every year, albeit with smaller 230 magnitudes than in 2020.

Data in 2020 and 2021 show that a similar CI processing mechanism also took place in the south polar vortex region at temperatures above 195 K. HCI in 2020 and 2021 continues to indicate

more active CI compared to other years at all temperatures until the temperature falls below 195 K, when the PSCs likely dominate the CI activation, and these two years merge into the 2004 – 235 2019 climatology. While CI activation in 2020 was lower at temperatures well below 195 K (Fig. 5F) compared to other years, this does not necessarily mean less total active CI being present in that year. In particular, the results show that a large amount of CI has already been activated earlier in the season (at warmer temperatures) and likely stayed in the forms of e.g. HOCI, CIO, and Cl<sub>2</sub>O<sub>2</sub> in the polar vortex region (6, 7). Because of less solar radiation at higher latitudes, less NO<sub>2</sub> is available from HNO<sub>3</sub> photochemistry to transfer these more reactivate forms of CI back to CIONO<sub>2</sub>. This is supported by the evidence of large non-zero values of the mean of PDFs for  $\Delta$ HCI+CIONO<sub>2</sub> at temperatures above 195 K in Fig. 5F (0.22 ± 0.12 ppb in 2020 and 0.18 ± 0.10 ppb in 2021, 243 compared to 0.02 ± 0.10 ppb in 2012; ± sign followed by 1 standard deviation).

Note that most of the ACE data points in the polar region are over  $65-70\,^{\circ}$ S (especially in colder seasons) and may not represent the conditions in the core of the polar vortex. Fig. S8 246 shows the limited data available for Cl activation between  $70-90\,^{\circ}$ S (ACE observations for March 247 and April only). The general behavior of Cl processing at warmer temperatures remains apparent 248 in these months at high latitudes.

# Altitude-dependent CI activation in the polar vortex region

The reaction efficiency of HCl+ClONO<sub>2</sub> can be affected not only by different types of 253 surfaces (e.g. organic aerosols and PSCs), but also by water vapor content and pressure, which 254 vary with altitude (34), which has been suggested as a potential mid-latitude ozone depletion 255 mechanism (35, 36). We therefore expand the focus to the range of altitudes from 14.5 km to 18.5 256 km for 2020, 2021 and 2012 (Fig. 6). Note that data quality may be affected at lower altitudes, with 257 more missing values at lower levels. An air parcel's recent minimum temperature exposure 258 becomes more sensitive to the number of days considered in back trajectories at lower altitudes, 259 where wind speed is slower, and the distance traveled by the air parcel might be too short to 260 adequately reflect the lowest temperature experienced by the parcel. Therefore, even in a reference 261 year in 2012, Fig. 6A shows Cl activation occurred at temperatures well above 195 K at altitudes

below 18.5 km. However, minimum temperatures from 5-day and 10-day back trajectories are not affected much at 18.5 km where wind speed is fast enough to allow air parcel to travel enough distance.

It is noteworthy that in a year without the impact of organic aerosols from large wildfires 266 (2012), a systematic gradient of the onset temperature for CI activation is indicated, from 200 K at 267 14.5 km to 195 K at 18.5 km using the 10-day back trajectories (Fig. 6D). This agrees surprisingly 268 well with current understanding, as indicated by a numerical calculation using the kinetics code and 269 composition data from WACCM (Whole Atmosphere Community Climate Model) (14). For example, 270 the reaction efficiency for HCI+CIONO2 is about 80 times more efficient at 14.5 km than at 18.5 km 271 (Fig. S9B), providing observational evidence for this effect in the atmosphere. But such altitude-272 dependency is significantly disturbed by organic aerosols after the 2020 Australian wildfire. Neither

2020 nor 2021 demonstrate a clear relationship between Cl activation and altitude. Instead, large amounts of Cl activation took place at all altitudes ranging from 14.5 km to 18.5 km in these years at temperatures warmer than 195 K.

#### **Discussion**

In conclusion, we have examined the heterogeneous reactions affecting the HCl and CIONO<sub>2</sub> reservoir species in the southern hemisphere fall and winter (March-July) for both the 281 Australian wildfire-released organic aerosols and background conditions using satellite data. Our 282 method confirms a sharp increase in Cl activation for temperatures below about 195 K along 5-day 283 air parcel trajectories characterizing the data, consistent with current understanding (11, 16, 37). 284 This finding highlights the importance of relatively small temperature perturbations (i.e., less than 1 K) on this chemistry (e.g., those due to planetary or gravity waves). The method also successfully

1 K) on this chemistry (e.g., those due to planetary or gravity waves). The method also successfully demonstrates the altitude-dependency of Cl activation for a reference non-wildfire year (34). These

results illustrate the power of this method for both background conditions and wildfire perturbations in testing chemical understanding.

We find evidence for CI processing at much warmer temperatures (above 220 K) than the current understanding for PSCs after the Australian fires. When such CI processing happens at 291 mid-latitudes, HCl decreases but nearly all of the active CI is turned into CIONO<sub>2</sub> rapidly because 292 of ongoing supply of NO<sub>2</sub> from HNO<sub>3</sub> photolysis and reaction with OH. However, PDFs of the sum

of HCI+CIONO2 activation reveal that some enhanced CI does remain in active forms at temperatures above 195 K in 2020, which can be expected to produce some ozone loss. 295 Importantly, the data suggest that the remaining aerosols from the 2020 wildfire apparently even continued to affect the CI species (albeit to a lesser extent) into 2021. Further, diversity in wildfire-released organic aerosols (17, 18) with different chemical properties is suggested by an observed increase in the width of the distribution, i.e., varying amounts of CI activation.

The total CI budget could be closed by including other species, particularly CIO and Cl<sub>2</sub>O<sub>2</sub>. However, one drawback of this tracer-tracer method is that it works well for the rather long-lived 301 species (e.g. HCl and CIONO<sub>2</sub>), but the large variance in more short-lived species (e.g. CIO and 302 HOCl) can impede the calculation. Furthermore, the ACE satellite produces twilight measurements 303 (which do not indicate daytime CIO values) and it does not have measurements for Cl<sub>2</sub>O<sub>2</sub>; although

(6) shows enhanced daytime CIO using MLS data, and twilight CIO enhancement is also found from ACE data albeit with larger noise (7). Further studies are needed to evaluate the total CI 306 budget and to fully quantify to what extent the ozone layer is affected by wildfire-triggered CI 307 processing. The frequency of wildfires is projected to increase in the future due to climate change (38). A better understanding of the range of composition of organic aerosols, and of heterogeneous reaction rates upon them, is needed to estimate any associated ozone impacts, including potential delay of the recovery in the stratospheric ozone layer in the future.

#### **Materials and Methods**

#### Satellite datasets

Level 2 satellite data from ACE-FTS (Atmospheric Chemistry Experiment-Fourier Transform Spectrometer) version 4.1 for molecules (39) is used in this study. Data range from 2004 to 2021. ACE provides measurements at twilight; both the sunrise and sunset data are used. We remove outliers defined as 3 standard deviations apart from the mean for each month (40).

Daily level 3 satellite data from MLS (Microwave Limb Sounder) version 5.0 (41) for N<sub>2</sub>O, HCl and temperature are used in this study. Data range from 2005 to 2021. Both the ascending and 323 descending modes are used, which provide measurements for daytime and nighttime.

#### **Back trajectory calculation**

Lagranto (Lagrangian Analysis Tool) version 2.0 (22) is used in this study to calculate the back trajectories for each data point in 2020, 2021, and 2012. It iterates three times in each time interval to calculate the average velocity between the starting and ending locations (from every iteration). Lagranto is driven by the ERA5 (European Centre for Medium-Range Weather Forecasts) reanalysis data (23) for pressure, temperature, and 3D wind fields. We used an ERA5 configuration that has 137 vertical model levels, a 1-degree horizontal resolution, and a 3-hour temporal resolution. Subgrid scale gravity waves can introduce temperature variability. ERA5 has been shown to resolve a large portion of that variability (42–44) and will be sampled irrespective of the time interval chosen for transport in the trajectory model. However, short horizontal wavelength disturbances could lead to effective chlorine activation at somewhat colder temperatures than those shown here, which should be considered an upper limit to the activation temperature.

### **HCI+CIONO**<sub>2</sub> reaction efficiency

The HCl+ClONO<sub>2</sub> reactive uptake probabilities (in Fig. S9B) are calculated using the 342 parameterization described in (14), which is used in the WACCM model. This calculation uses model values of temperature and pressure over an altitude range of 14.5–19.5 km during July at ~63°S. HCl and ClONO<sub>2</sub> volume mixing ratios are held constant at 0.3 and 0.05 ppb respectively. Water vapor volume mixing ratio is held constant at 3.5, 4, and 4.5 ppm. This allows for the effect of water vapor partial pressure over the above altitude to range to be investigated.

347 348 349

## Data availability

350 351

Data and code used in this study are available at https://doi.org/10.5281/zenodo.7338322 (45).

352 353

## **Acknowledgments**

354 355

The authors appreciate Hongwei Sun (Harvard University) for the guidance in using Lagranto. SS, PW, and KS gratefully acknowledge partial support by NSF-1906719 and NASA 80NSSC19K0952. We thank P. F. Bernath, Mission Scientist of the Atmospheric Chemistry Experiment. ACE is 358 supported by the Canadian Space Agency (which makes ACE data freely available).

359 360 361

356

357

#### References

- 1. D. A. Peterson, *et al.*, Australia's Black Summer pyrocumulonimbus super outbreak reveals potential for increasingly extreme stratospheric smoke events. *npj Clim Atmos Sci* **4**, 38 (2021).
- G. D'Angelo, S. Guimond, J. Reisner, D. A. Peterson, M. Dubey, Contrasting Stratospheric Smoke
   Mass and Lifetime From 2017 Canadian and 2019/2020 Australian Megafires: Global Simulations
   and Satellite Observations. *JGR Atmospheres* 127 (2022).
- 3. T. Deshler, *et al.*, Trends in the nonvolcanic component of stratospheric aerosol over the period 1971–2004. *J. Geophys. Res.* **111**, D01201 (2006).
- P. Yu, et al., Persistent Stratospheric Warming Due to 2019–2020 Australian Wildfire Smoke.
   Geophys Res Lett 48 (2021).
- L. A. Rieger, W. J. Randel, A. E. Bourassa, S. Solomon, Stratospheric Temperature and Ozone
   Anomalies Associated With the 2020 Australian New Year Fires. *Geophysical Research Letters* 48
   (2021).
- M. L. Santee, et al., Prolonged and Pervasive Perturbations in the Composition of the Southern
   Hemisphere Midlatitude Lower Stratosphere From the Australian New Year's Fires. Geophysical
   Research Letters 49 (2022).
- P. Bernath, C. Boone, J. Crouse, Wildfire smoke destroys stratospheric ozone. *Science* 375, 1292–
   1295 (2022).
- 381 8. A. R. Klekociuk, *et al.*, The Antarctic ozone hole during 2020. *J. South. Hemisph. Earth Syst. Sci.* **72**, 382 19–37 (2022).

- 383 9. A. Ansmann, *et al.*, Ozone depletion in the Arctic and Antarctic stratosphere induced by wildfire smoke. *Atmos. Chem. Phys.* **22**, 11701–11726 (2022).
- 385 10. S. E. Strahan, *et al.*, Unexpected Repartitioning of Stratospheric Inorganic Chlorine After the 2020 Australian Wildfires. *Geophysical Research Letters* **49** (2022).
- 387 11. S. Solomon, R. R. Garcia, F. S. Rowland, D. J. Wuebbles, On the depletion of Antarctic ozone. 4 (1986).
- 389 12. S. Solomon, *et al.*, On the stratospheric chemistry of midlatitude wildfire smoke. *Proc. Natl. Acad.* 390 *Sci. U.S.A.* **119**, e2117325119 (2022).
- 391 13. D. R. Hanson, A. R. Ravishankara, Uptake of hydrochloric acid and hypochlorous acid onto sulfuric acid: solubilities, diffusivities, and reaction. *J. Phys. Chem.* **97**, 12309–12319 (1993).
- 393 14. Q. Shi, J. T. Jayne, C. E. Kolb, D. R. Worsnop, P. Davidovits, Kinetic model for reaction of ClONO <sub>2</sub>
  394 with H <sub>2</sub> O and HCl and HOCl with HCl in sulfuric acid solutions. *J. Geophys. Res.* **106**, 24259–24274
  395 (2001).
- 396 15. S. R. Kawa, *et al.*, Activation of chlorine in sulfate aerosol as inferred from aircraft observations. *J. Geophys. Res.* **102**, 3921–3933 (1997).
- 398 16. S. Solomon, D. Kinnison, J. Bandoro, R. Garcia, Simulation of polar ozone depletion: An update. *J. Geophys. Res. Atmos.* **120**, 7958–7974 (2015).
- 400 17. C. D. Boone, P. F. Bernath, M. D. Fromm, Pyrocumulonimbus Stratospheric Plume Injections 401 Measured by the ACE-FTS. *Geophys. Res. Lett.* **47** (2020).
- 402 18. D. M. Murphy, *et al.*, Radiative and chemical implications of the size and composition of aerosol particles in the existing or modified global stratosphere. *Atmos. Chem. Phys.* **21**, 8915–8932 (2021).
- 404 19. J. R. Lawrence, S. V. Glass, S.-C. Park, G. M. Nathanson, Surfactant Control of Gas Uptake: Effect of Butanol Films on HCl and HBr Entry into Supercooled Sulfuric Acid. *J. Phys. Chem. A* **109**, 7458–7465 406 (2005).
- 407 20. Y. Q. Li, *et al.*, Uptake of HCl(g) and HBr(g) on Ethylene Glycol Surfaces as a Function of Relative Humidity and Temperature. *J. Phys. Chem. A* **106**, 1220–1227 (2002).
- 409 21. P. F. Bernath, Atmospheric Chemistry Experiment (ACE): Mission overview. *Geophys. Res. Lett.* **32**, 410 L15S01 (2005).
- 411 22. M. Sprenger, H. Wernli, The LAGRANTO Lagrangian analysis tool version 2.0. *Geosci. Model Dev.* **8**, 412 2569–2586 (2015).
- 413 23. H. Hersbach, et al., The ERA5 global reanalysis. Q.J.R. Meteorol. Soc. 146, 1999–2049 (2020).
- 414 24. M. P. Chipperfield, *et al.*, On the use of HF as a reference for the comparison of stratospheric observations and models. *J. Geophys. Res.* **102**, 12901–12919 (1997).

- 416 25. S. Tilmes, R. Müller, J.-U. Grooß, J. M. Russell III, Ozone loss and chlorine activation in the Arctic winters 1991-2003 derived with the tracer-tracer correlations. *Atmos. Chem. Phys.* **4**, 2181–2213 (2004).
- 419 26. M. H. Proffitt, S. Solomon, M. Loewenstein, Comparison of 2-D model simulations of ozone and nitrous oxide at high latitudes with stratospheric measurements. *J. Geophys. Res.* **97**, 939 (1992).
- 421 27. M. H. Proffitt, *et al.*, Ozone loss in the Arctic polar vortex inferred from high-altitude aircraft measurements. *Nature* **347**, 31–36 (1990).
- 423 28. D. Griffin, *et al.*, Stratospheric ozone loss in the Arctic winters between 2005 and 2013 derived with 424 ACE-FTS measurements. *Atmos. Chem. Phys.* **19**, 577–601 (2019).
- 425 29. N. J. Livesey, *et al.*, Investigation and amelioration of long-term instrumental drifts in water vapor and nitrous oxide measurements from the Aura Microwave Limb Sounder (MLS) and their implications for studies of variability and trends. *Atmos. Chem. Phys.* **21**, 15409–15430 (2021).
- 428 30. M. P. Chipperfield, E. R. Lutman, J. A. Kettleborough, J. A. Pyle, A. E. Roche, Model studies of chlorine deactivation and formation of ClONO 2 collar in the Arctic polar vortex. *J. Geophys. Res.* 430 **102**, 1467–1478 (1997).
- 431 31. D. L. Hartmann, J. R. Holton, Q. Fu, The heat balance of the tropical tropopause, cirrus, and stratospheric dehydration. *Geophys. Res. Lett.* **28**, 1969–1972 (2001).
- 433 32. M. G. Mlynczak, C. J. Mertens, R. R. Garcia, R. W. Portmann, A detailed evaluation of the stratospheric heat budget: 2. Global radiation balance and diabatic circulations. *J. Geophys. Res.* 435 **104**, 6039–6066 (1999).
- 436 33. G. P. Schill, *et al.*, Widespread biomass burning smoke throughout the remote troposphere. *Nat.* 437 *Geosci.* **13**, 422–427 (2020).
- 438 34. S. Solomon, Stratospheric ozone depletion: A review of concepts and history. *Rev. Geophys.* **37**, 439 275–316 (1999).
- 440 35. J. G. Anderson, *et al.*, Stratospheric ozone over the United States in summer linked to observations of convection and temperature via chlorine and bromine catalysis. *Proc. Natl. Acad. Sci. U.S.A.* **114** 442 (2017).
- 443 36. C. E. Clapp, J. G. Anderson, Modeling the Effect of Potential Nitric Acid Removal During Convective 444 Injection of Water Vapor Over the Central United States on the Chemical Composition of the Lower 445 Stratosphere. *JGR Atmospheres* **124**, 9743–9770 (2019).
- 446 37. D. M. Wilmouth, *et al.*, Evolution of inorganic chlorine partitioning in the Arctic polar vortex. *J. Geophys. Res.* **111**, D16308 (2006).
- 448 38. S. I. Seneviratne, X. Zhang, "Chapter 11: Weather and Climate Extreme Events in a Changing Climate (IPCC sixth assessment report)" (WMO/UNEP).
- 450 39. C. D. Boone, *et al.*, Retrievals for the atmospheric chemistry experiment Fourier-transform spectrometer. *Appl. Opt.* **44**, 7218 (2005).

452 453	40.	C. Boone, Data usage guide and file format description for ACE-FTS level 2 data version 4.1 ASCII format (2020) (August 2, 2022).
454	41.	N. Livesey, et al., Version 5.0x Level 2 and 3 data quality T S and description document (2022).
455 456 567–59		A. Dörnbrack, S. D. Eckermann, B. P. Williams, J. Haggerty, Stratospheric Gravity Waves Excited by a Propagating Rossby Wave Train—A DEEPWAVE Case Study. <i>Journal of the Atmospheric Sciences</i> <b>79</b> , 457 (22).
458 459	43.	A. Dörnbrack, et al., Unusual appearance of mother-of-pearl clouds above El Calafate, Argentina (50°21'S, 72°16'W). Weather <b>75</b> , 378–388 (2020).
460 461	44.	A. Dörnbrack, tratospheric Mountain Waves Trailing across Northern Europe. <i>Journal of the Atmospheric Sciences</i> <b>78</b> , 2835–2857 (2021).
462 463	45.	P. Wang, S. Solomon, K. Stone, Data and code for "Stratospheric chlorine processing after the 2020 Australian wildfires derived from satellite data" (2022).
464		
465		

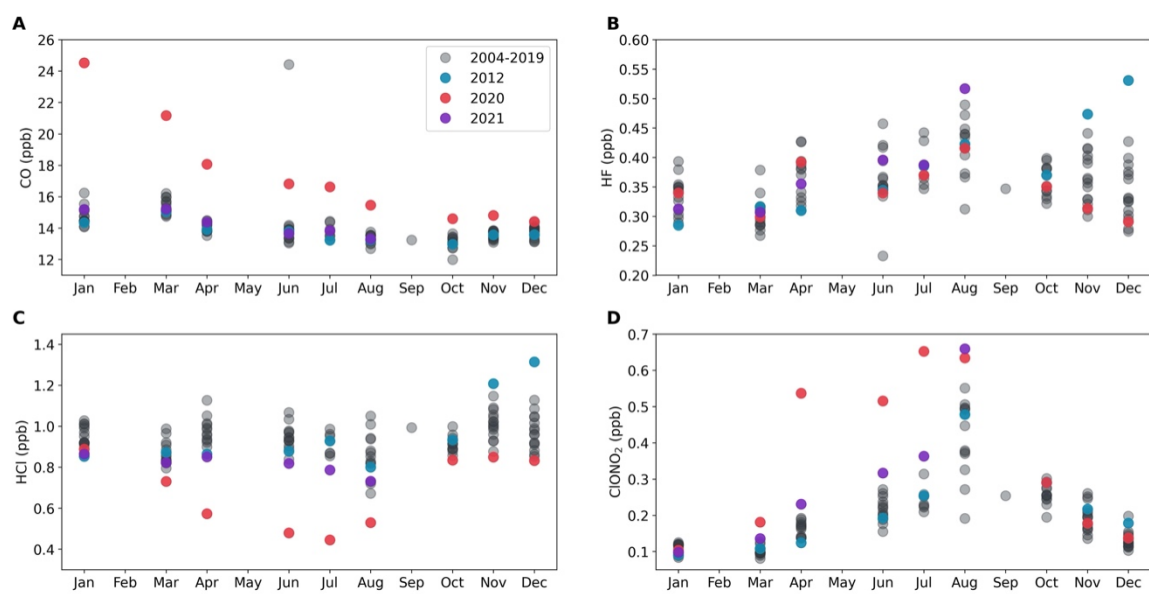


**Fig. 1.** The monthly mean ACE data for (A) CO, (B) HF, (C) HCl, and (D) ClONO<sub>2</sub> at 18.5 km averaged over 40 - 55 °S. Red dots are from 2020, purple dots are from 2021, blue dots are from 2012 (used as a reference year in this study), and gray dots are from 2004 – 2019 (excluding 2012). 40 - 55 °S is split into 3 equally spaced latitude bins and months with at least 5 samples (at least 471 1 sample per latitude bin) are considered in the averaging processes.

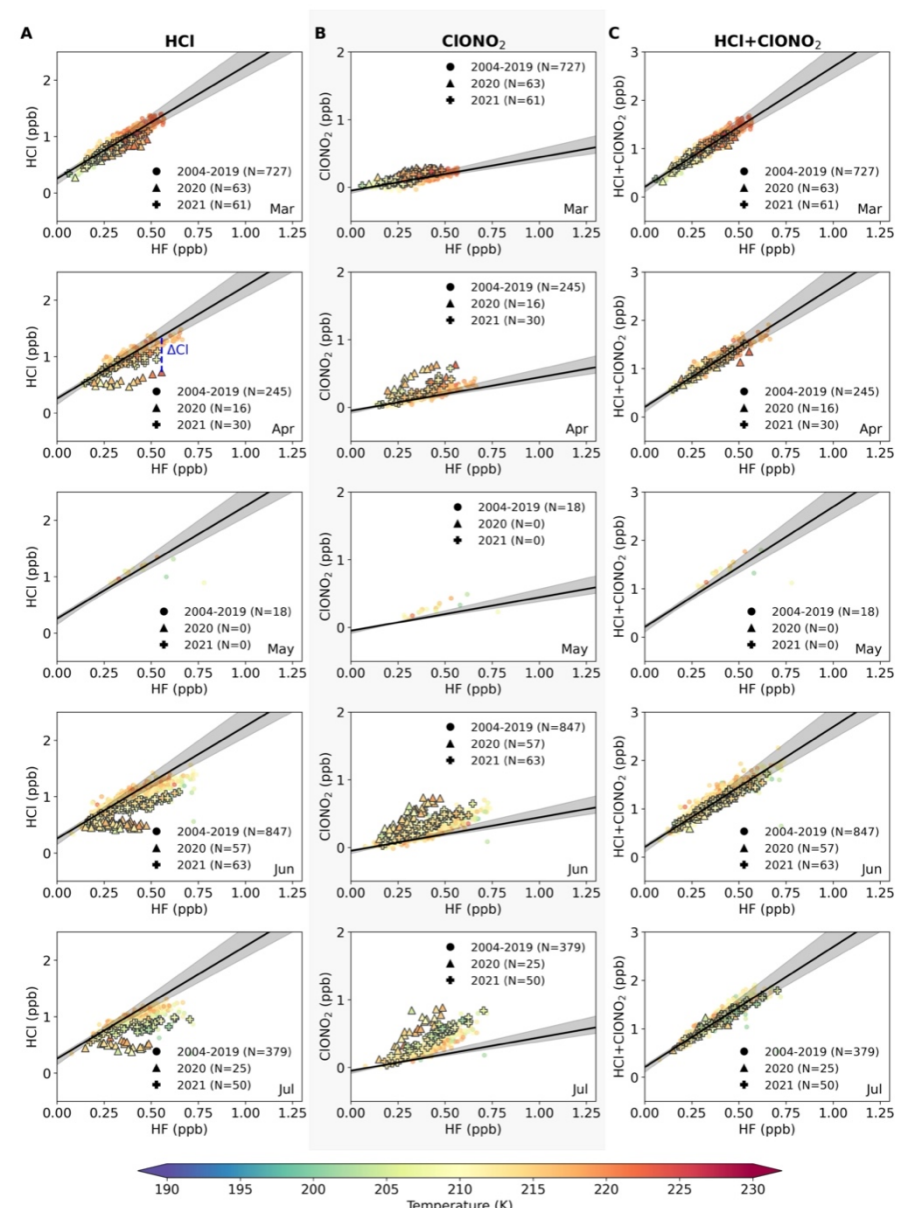


**Fig. 2.** Tracer-tracer correlation between HF (x-axis) and (A) HCl, (B) ClONO<sub>2</sub>, and (C) 474 HCl+ClONO<sub>2</sub> (y-axes), color-coded by temperature. Each dot represents a single measurement at 18.5 km over 40-55 °S. Dots in 2020 and 2021 are highlighted with triangles and crosses, 476 respectively (with gray edges). Each subpanel shows a different month from March to July, labeled at the bottom right corner. The number of data plotted in each month is shown in the legend. The thick black lines represent the "no-chemistry" baseline, from the linear fit over March 2004 – 2019 data points. The shaded regions indicate a conservative full range of baseline variability bounded by the maximum and minimum baselines constructed by data in individual years from 2004 to 2019. A demonstration of how ΔCI (e.g. in Fig. 4) is calculated is shown here as the vertical blue dashed line in the April panel for HCI, representing the change in CI due to chemical processes.

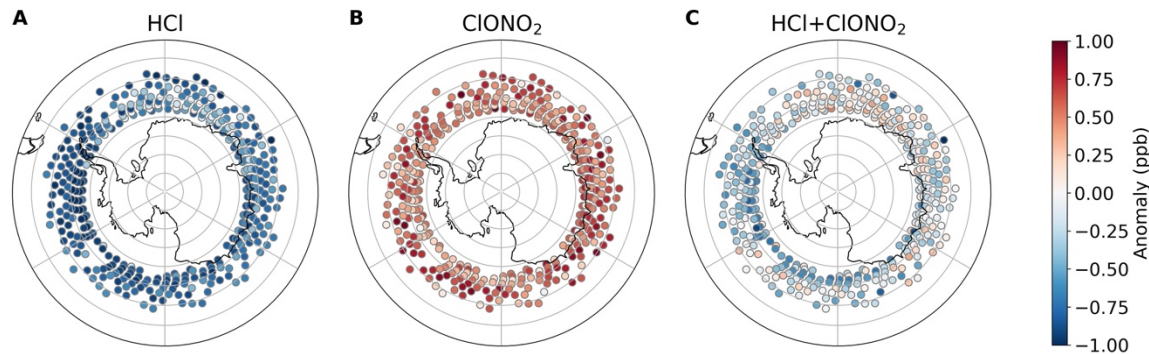


**Fig. 3.** Monthly anomalies for (A) HCl, (B) ClONO<sub>2</sub>, and (C) HCl+ClONO<sub>2</sub> in May 2020 compared to the May climatology in 2004-2019. The maps show a latitudinal range between 50 °S and 90 °S since ACE measurements in May are mainly between 58-68 °S. To prevent from biasing the 487 anomalies by latitudinal variations, the climatological mean is constructed at every 5-degree latitude bin. Therefore, the May anomalies presented here are calculated from four latitude bins from the climatology (50-55, 55-60, 60-65 and 65-70 °S).

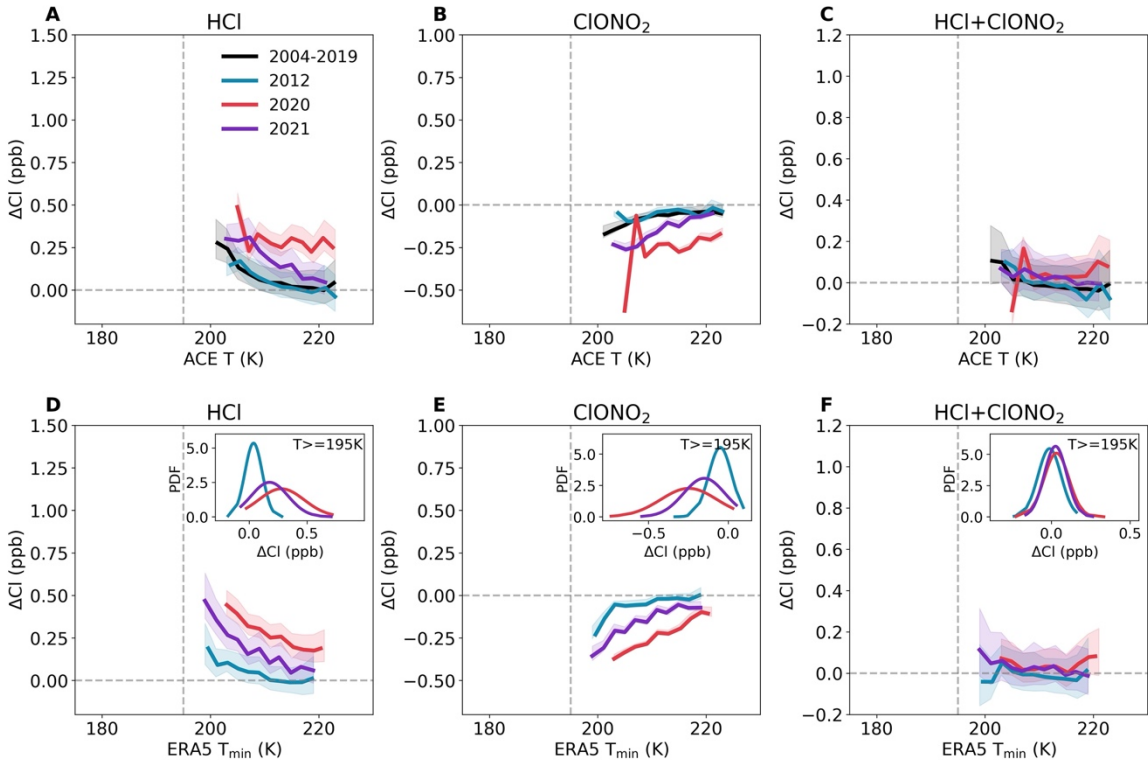


**Fig. 4.** Cl activation as a function of temperature at mid-latitudes  $(40 - 55 \, ^{\circ}\text{S})$  for March-July at 18.5 km. Each panel shows the amount of Cl activation on the y-axes (deviation from the "no-493 chemistry" baseline in Fig. 2) as a function of temperature (x-axis) for (A, D) HCl, (B, E) ClONO<sub>2</sub>, and (C, F) HCl+ClONO<sub>2</sub>. Panels A-C use the ACE-measured temperature at the satellite overpass, and panels D-F use the minimum temperature ( $T_{min}$ ) calculated along the 5-day back trajectories for each data point for 2020, 2021, and 2012. Thick lines are the average of Cl activation at every 2 K temperature ranges (temperature bins with less than 2 samples are not considered for the 498 average). The shading areas indicate the full range of Cl departures from individual baselines using data from single years. Horizontal and vertical gray dashed lines indicate zero Cl activation and 195 K, respectively. The probability distribution functions (PDF) of Cl activation at  $T_{min} >= 195 \, \text{K}$  are shown in panels D-F for 2020, 2021, and 2012.

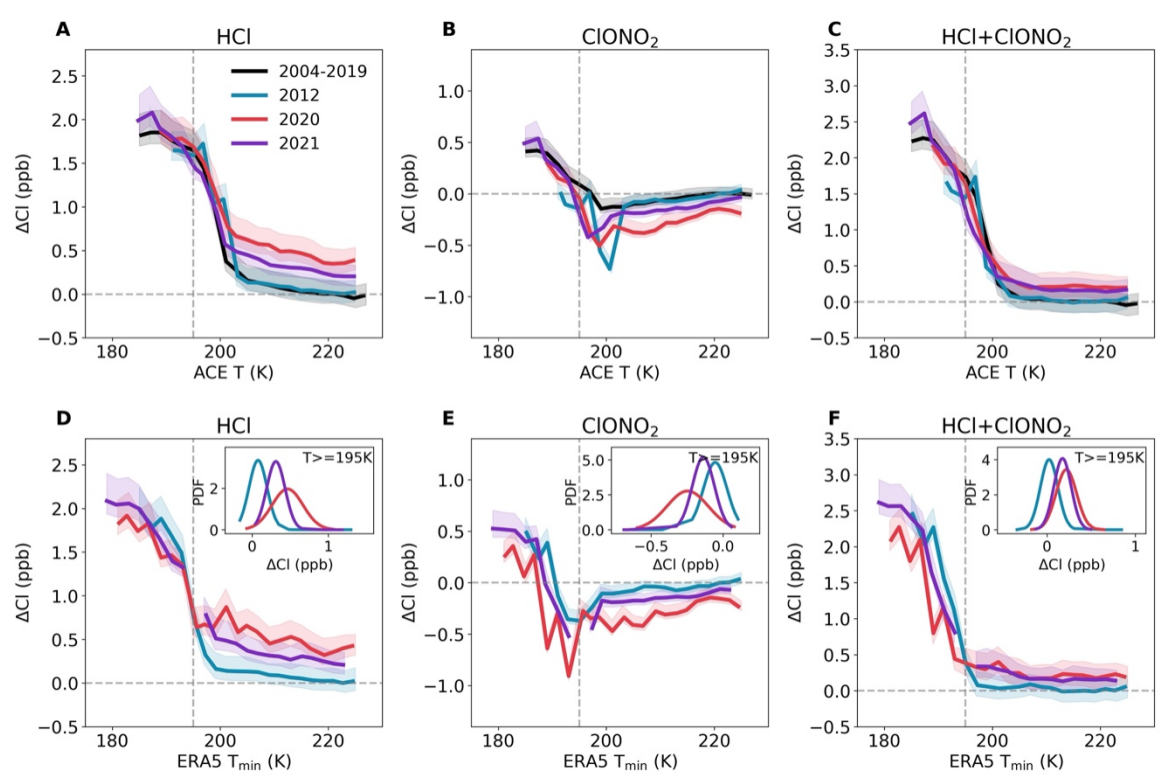


**Fig. 5.** Cl activation as a function of temperature in the polar vortex region (65 – 90 °S), as in Fig. 4 for mid-latitudes. Panels A-C use the ACE-measured temperature at the satellite overpass, and panels D-F use the minimum temperature ( $T_{min}$ ) calculated along the 5-day back trajectories for each data point for 2020, 2021, and 2012.

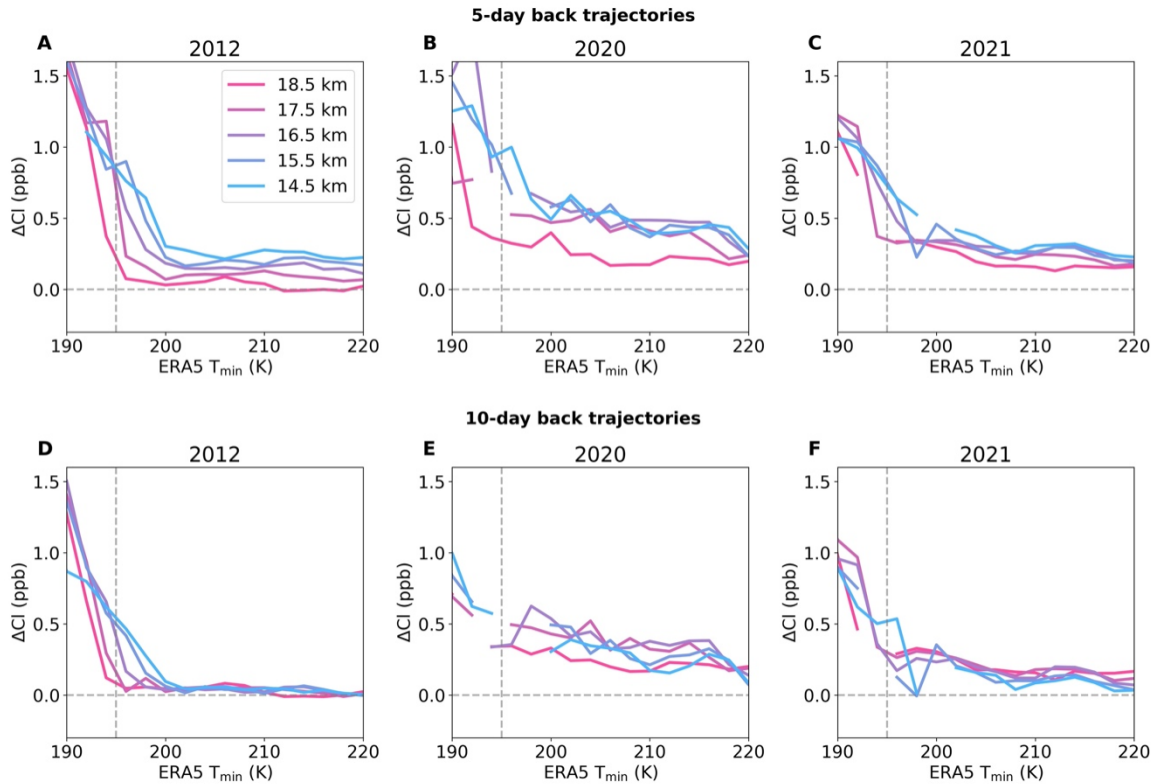


**Fig. 6.** The altitude-dependent Cl activation in the polar vortex region  $(65-90\,^\circ\text{S})$  for  $(A,\,D)$  2012,  $(B,\,E)$  2020, and  $(C,\,F)$  2021. X-axis shows the minimum temperature calculated along the 5-day back trajectories (panels A-C) and 10-day back (panels D-F), and the y-axis shows the Cl activation from the sum of HCl and ClONO2. Only the Cl activation calculated from baselines using all 512 available data from 2004 to 2019 is shown here. Each line represents a different altitude range from 14.5 km to 18.5 km. The panels are zoomed in for 190 – 220 K to focus on the onset 514 temperature for Cl activation on PSCs.

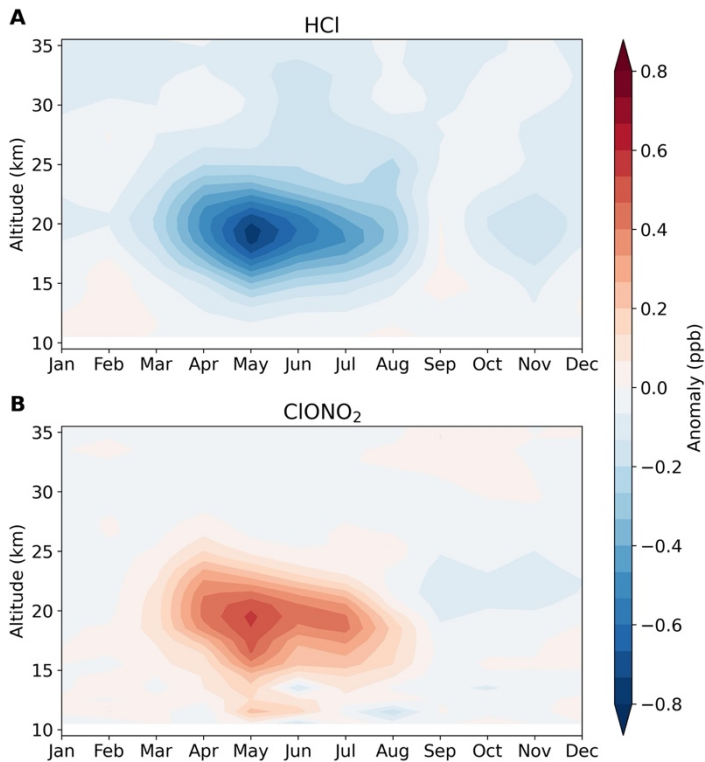
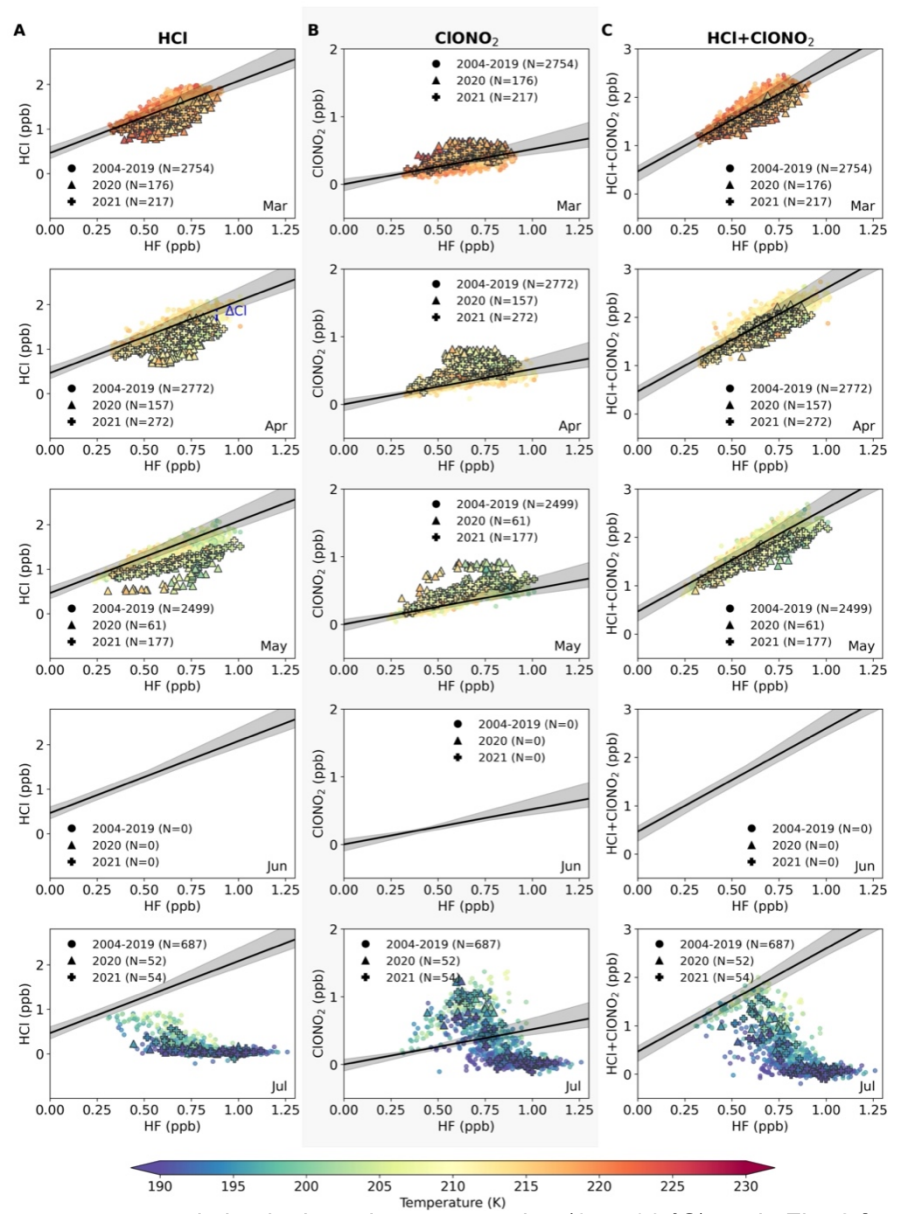
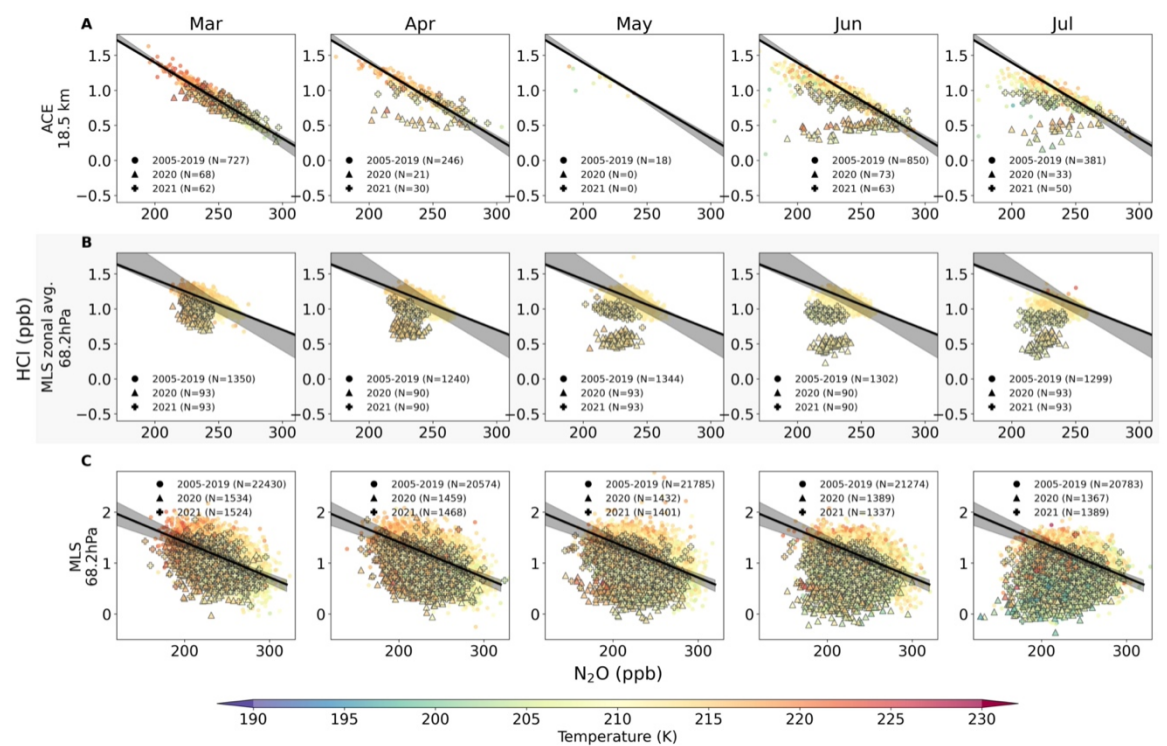


Fig. S1. Monthly anomalies of (A) HCl and (B) ClONO<sub>2</sub> in 2020 compared to the 2004 – 2019 climatology, as a function of the month (x-axis) and altitude (y-axis) over 40 – 60 °S.



**Fig. S2.** Tracer-tracer correlation in the polar vortex region  $(65 - 90 \degree S)$ , as in Fig. 2 for midlatitudes. There is no data in June at this latitude range.



**Fig. S3.** Tracer-tracer correlation between  $N_2O$  (x-axis) and HCl (y-axis) in the mid-latitude (40 – 55 °S), similar to Fig. 2, but comparing ACE and MLS measurements in each row. Top row (panel A) shows results from ACE individual measurements at 18.5 km. Middle row (panel B) shows results from MLS zonally averaged data at 68.2 hPa. Bottom row (panel C) shows results from MLS individual measurements at 68.2 hPa.

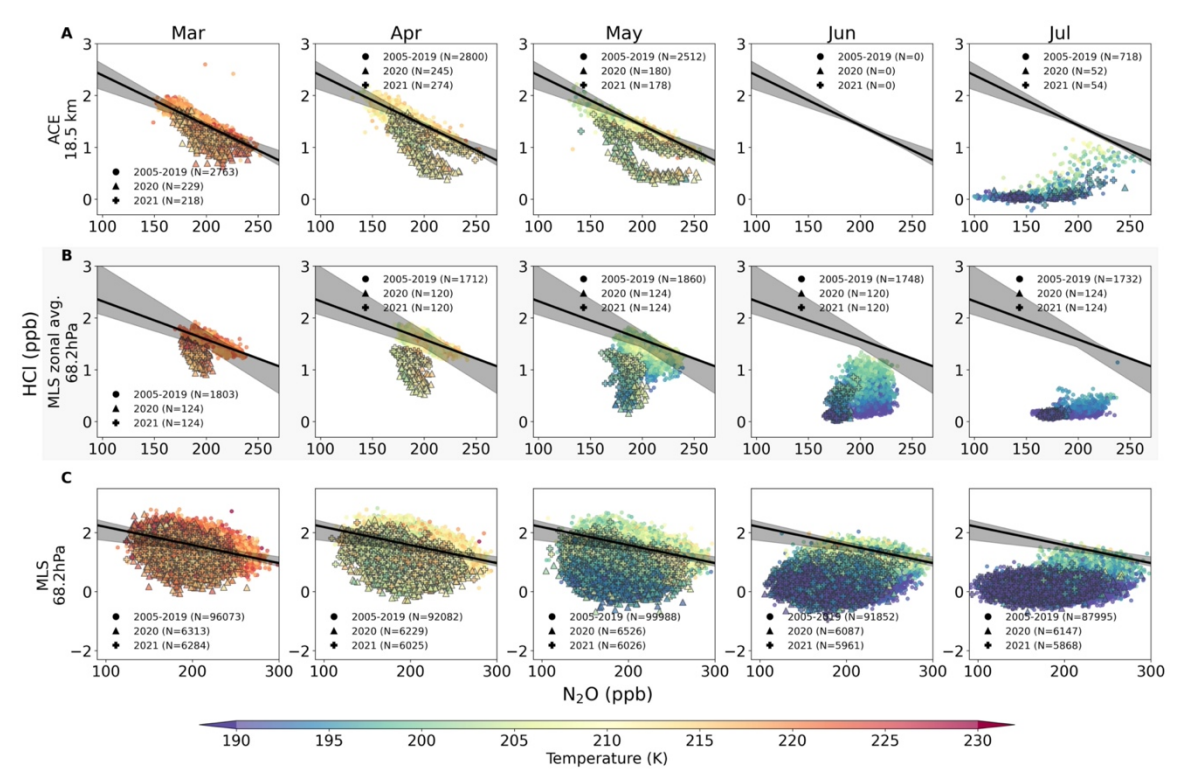
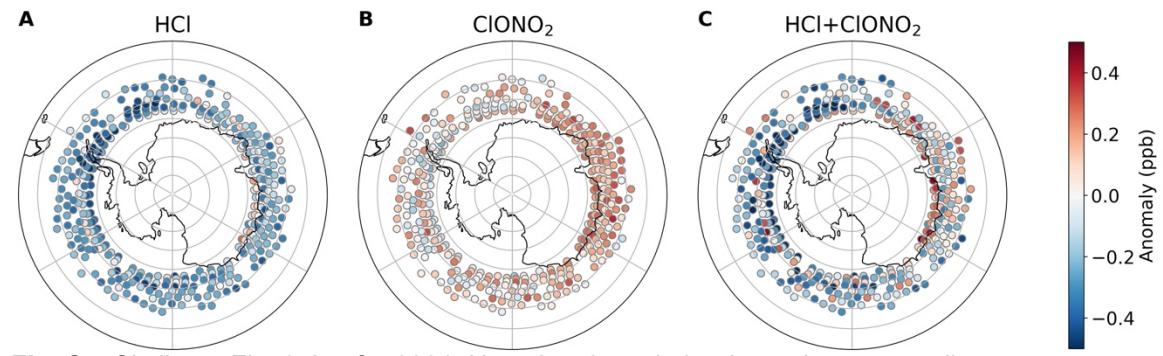
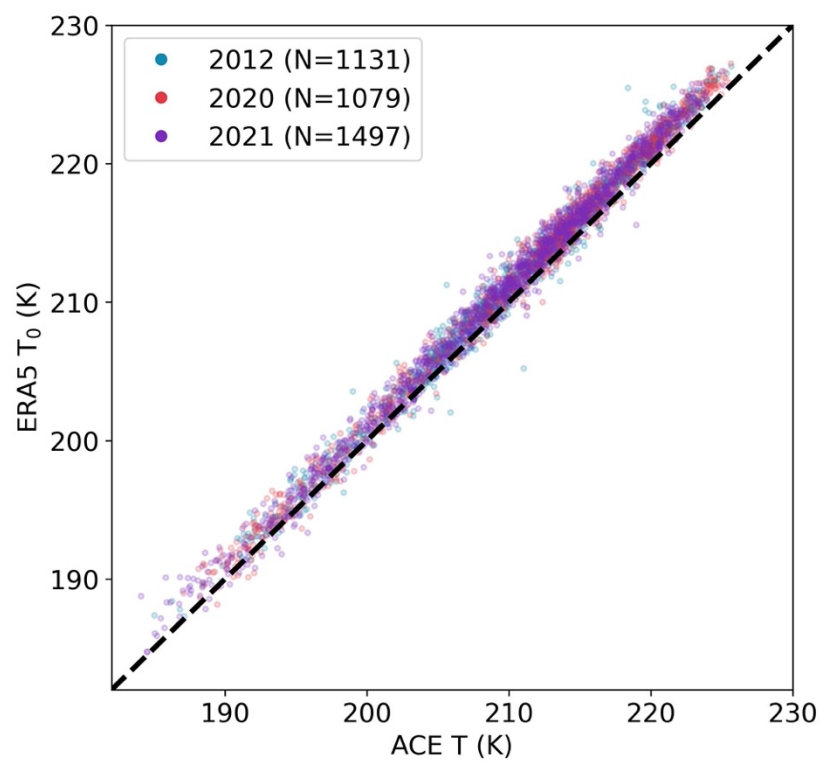


Fig. S4. Tracer-tracer correlation between  $N_2O$  (x-axis) and HCl (y-axis) in the polar vortex region (65 – 90 °S), as in Fig. S3 for mid-latitudes.





**Fig. S5.** Similar to Fig. 3, but for 2021. Note that the colorbar here shows a smaller range because the magnitude of the Cly anomalies are smaller in 2021.



**Fig. S6.** Sanity check on ACE and ERA5 temperature at 18.5 km. X-axis shows the ACE-observed temperature (ACE T), and the y-axis shows the ERA5 temperature at the closest rounded location and time with ACE satellite overpass (ERA5  $T_0$ ) for individual data points in 2020 (red), 2021 538 (purple), and 2012 (blue) over the full latitude range we use in this study (40 – 90 °S). The black 539 dotted line indicates the 1-1 ratio. The total coefficient of determination  $R^2$  value for ACE T and 540 ERA5  $T_0$  (concatenating all three years) is 0.97, with a mean bias of 1.1 K.

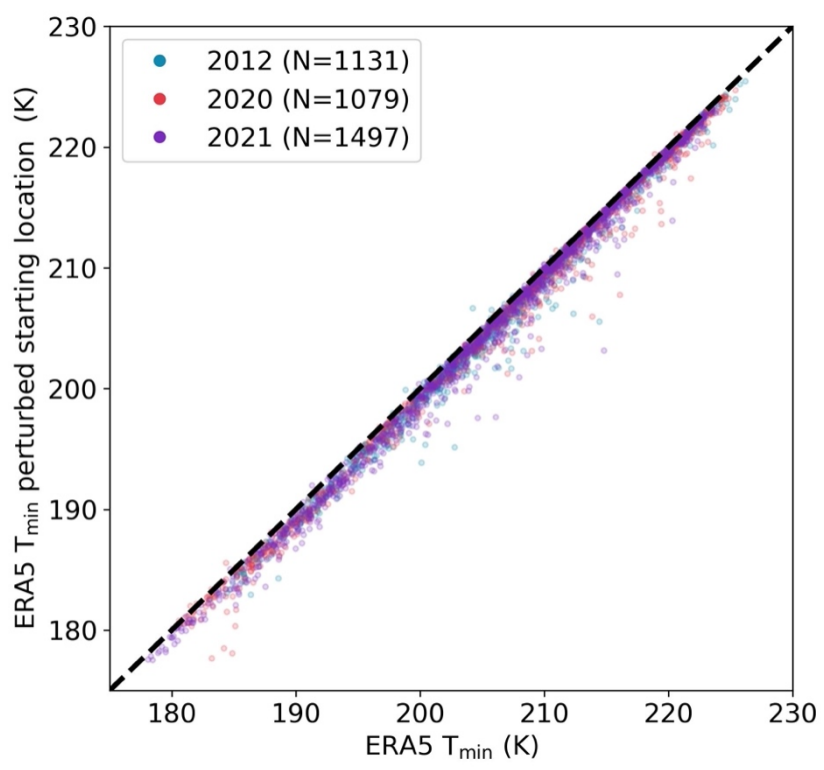


**Fig. S7.** Sensitivity test for the back trajectory calculation at different starting locations at 18.5 km. X-axis shows the minimum temperature from the 5-day back trajectory starting at the closest 544 latitude/longitude from ACE observation. Y-axis shows a similar 5-day minimum temperature from back trajectory calculations but for data points released at  $\pm$  1 degree latitude and longitude from the satellite overpass location. The dashed black line indicates the 1-1 ratio. With such 547 perturbations in the starting location,  $T_{\text{min}}$  can have a mean bias at -0.8 K.

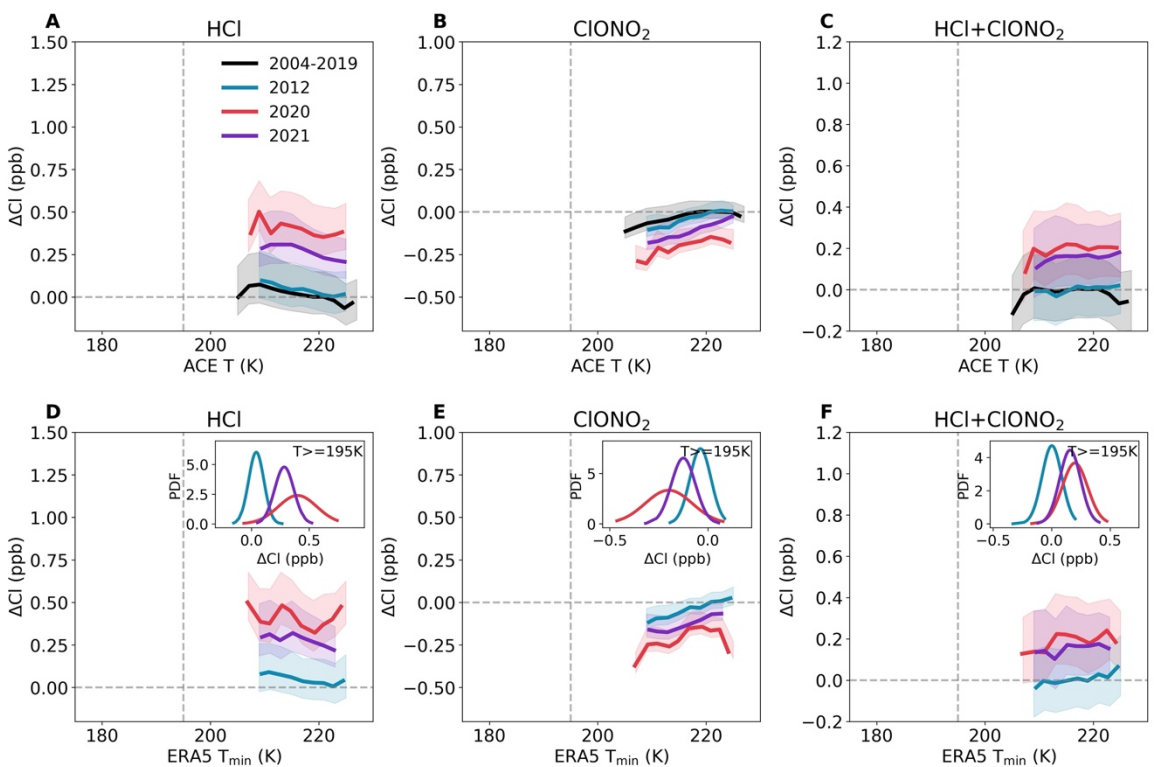


**Fig. S8.** Cl activation as a function of temperature at the core of the polar vortex region  $(70 - 90 \, ^\circ\text{S})$ . Most of the data points in Fig. 5 are over  $65 - 70 \, ^\circ\text{S}$ , which might not represent the behaviors within the core of polar vortex. This figure shows data points over  $70 - 90 \, ^\circ\text{S}$ , where data is only 553 available in March and April (when temperatures are well above 200 K).

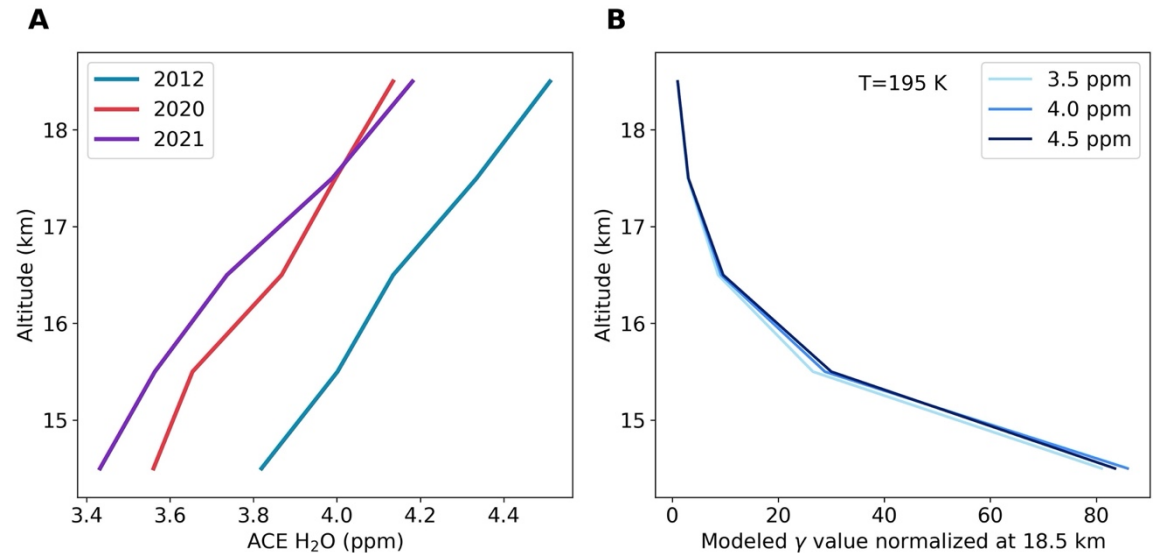


**Fig. S9.** (*A*) shows the ACE measured July H<sub>2</sub>O in the polar vortex region (65 – 90 °S) at different altitudes from 14.5 km to 18.5 km. The spread of H<sub>2</sub>O is around 3.5 ppm to 4.5 ppm. (*B*) shows the γ value (reaction efficiency of HCl+ClONO<sub>2</sub>) calculated from a similar parameterization used in WACCM at a fixed temperature of 195 K at different altitudes. γ values are normalized as ratios compared to the reaction efficiency at 18.5 km. An adopted spread in H<sub>2</sub>O volume mixing ratio of  $\pm$ 0.5 ppm from 4 ppm is shown in panel *B*, illustrating that water vapor mixing ratio has a small 561 effect on the reaction efficiency, while pressure plays a dominating role for the background 562 condition. At lower altitudes (high pressure), the efficiency of the HCl+ClONO<sub>2</sub> reaction is 563 significantly enhanced compared to higher altitudes (low pressure).